A robotic arm to sort different types of ball bearings from the knowledge discovered by size measurements of image regions and RFID support

Nicola Ivan Giannoccaro*, Luigi Spedicato, Aimè Lay-Ekuakille
Dipartimento di Ingegneria dell'Innovazione, Universita del Salento
via per Monteroni 73100 Lecce, Italy
* corresponding author ; email: ivan.giannoccaro@unisalento.it; Tel. +390832297813

Submitted: Mar. 15, 2014 ***Accepted: May 5, 2014*** ***Published: June 1, 2014***

Abstract- In this paper, the authors present a mechatronics system consisting of an intelligent robotic arm able to sort ball bearings having the same colour and shape drawing advantage from vision. After acquiring and processing an image from a camera, two almost concentric and circular regions are extracted from the image and their areas are calculated as number of pixels belonging to them. The center of these regions provides the point that the end-effector has to reach in order to grip a cylindrical transport structure where the bearing is placed. Since the size measurements of image regions are very repeatable and the depth between the camera and the object is known, the bearing is recognized from the area. For the sake of automatically appreciating the effectiveness of the proposed approach, a RFID (Radio-Frequency Identification) tag is attached to the transport structure that supports the object. The tag contains stored information on the specific bearing for verifying the success in recognition making use of a reader device. Several experimental tests confirmed that the suggested strategy may be applied to track spare parts in assembly lines.

Index terms*: Planning of trajectories, Image processing, Pattern recognition, RFID technology.*

I. INTRODUCTION

During the last years, rapid progresses in technologies have influenced robotic systems that make use of innovative sensors able to provide useful information on the explored environment. These systems process sensory information with a view of controlling actuators and of attempting given tasks according to appropriate decisions made by computational units. The most important, inexpensive and popular sensors consist in cameras that may capture digital images for computer vision, that is the scientific approach to investigate how artificial vision technologies can be achieved. In consequence of the great impact of digital images on modern robotics, image processing has become the crucial problem for accurate detection of patterns from the image and for recognition. Image processing and recognition arise as separate topics but they are closely related. The field of image processing is mainly concerned with conversion, filtering and enhancement of images. On the other hand, the area of pattern recognition above all consists of feature extraction and classification. Considerable growth of interest in problems of recognition has brought into being an increasing need of theoretical methods and the majority of them rely on shape measurements of extracted image regions. The early and commonly used techniques lay in calculating Hu moment invariants as descriptors that are independent from linear transformations such as scaling, shifting and rotation [1-3]. Lately, many approaches based on moment invariants have been introduced in scientific literature [4-8] and pattern recognition has become an important research area. Researchers have also concentred their attention on real object recognition under changing viewpoints and illumination [9]. Moreover, some works concern with a new set of invariants, such as Zernike moments [10,11], Quaternion Zernike moments [12], Legendre moments [13,14] and radial Chebychev moments [15,16]. When objects have different colour, the aim of recognition is simplified because colour features can be extracted to differentiate them [17]. Robots can avail themselves of colour information: for example, a robotic arm, similar to that herein considered, is used to sort coloured cubes in [18] and a SCARA robot is driven to sort various coloured products in [19]. In this paper, the authors deal with a more complex recognition problem that arises from target objects characterized by the same shape and the same colour. The contribution of this work is to propose an automatic sorting of ball bearings that can be solely distinguished from their size. The acquired RGB image is converted into grayscale by eliminating the hue and saturation information. Then, the obtained image is converted to black and white. This

aim is achieved by choosing a suitable threshold on the pixel values in such a way as to have a binary image. For the sake of extracting the regions relating to the target ball bearing, all the connected components, that have fewer than an appropriate value of pixels, are removed. Moreover, morphological closing with a disk structuring element permits to preserve the shape of the target object by smoothening its edge. In this way, two almost concentric and circular regions are traced and the area is calculated as number of pixels belonging to each region. Different images were acquired for each ball bearing and the area features were gathered in a database. Finally, the recognition goal could be achieved by matching the area features obtained from a new test image with the stored data. Successively, the depth between camera and object was changed in a small range and a suitable relationship between the depth camera-object and the area was drawn to generalize the proposed approach. In order to verify invariance for all the considered ring-shaped objects, the seven Hu moment invariants [1-3] and the Flusser and Suk invariant [4,6,8] were also calculated and examined. The critical aspect of this method is the threshold choice to convert the grayscale image into binary. The threshold strictly depends on the environmental brilliance that is the reason why the authors chose to make use of neon lighting so as to assure the correct extraction of each image region. In order to test the sensitivity to light variations, the authors also decided to switch off the artificial light and to carry out experiments with sun lighting. In this experimental condition, the previous choice for the threshold did not always allow the extraction of the two expected regions. One RFID tag was glued on the base of each transport structure to automatically detect the success in recognition. In case the almost concentric and circular regions were extracted, the robotic arm was driven to catch the structure by moving the end-effector at the point obtained from the centroids of these regions. Successively, the robotic arm could take the tag above a reader at a short distance for identification. Therefore, the object lying on the considered structure could be directly detected from the linked information. The arm was able to deliver the transport structure to an assigned deposit location into the work space. Different locations were attributed to all ball bearings and several experimental tests were executed to appreciate the effectiveness of the suggested technique. The realized system is an example of integration between camera feedback and RFID technology for automatic sorting of objects. All the technical aspects on the proposed application will be given later on.

II. THE SMART ROBOTIC ARM

The robotic arm Lynxmotion AL5C [20] (Fig. 1a) was utilized to sort ball bearings according to the information collected from the camera and from RFID. In a previous work, the considered robotic arm was proposed for environmental protection by automatizing the process of waste stocking [21]. The arm is made up of five servo-motors that assure accurate and repetitive movements: two servos HS-485HB for the base rotation and the wrist respectively, one servo HS-755HB for the shoulder and one servo HS-645MG for the elbow. The end-effector is a gripper that may be open or closed by driving a further servo motor HS-422. This actuator allows to grab the transport structure maintaining an upright position. The robotic arm is able to deliver fast, very accurate and repeatable movements. The powerful servo motors offer a wide rotation and they may be connected to the I/O bus of the servo controller SSC32 [20]. This controller was used in the experimental tests to drive the servo motors by a computer and to move one or more servo-motors according to given code instructions. For the purpose of operating wirelessly, the data and power cables of a Bluetooth Modem BlueSMiRF [20] were connected to the SSC32 module and a bluetooth USB dongle was plugged into a spare USB port on the computer. In this way, the reliable communication was assured by a ceramic antenna and the desired joint angles could be defined by setting the addresses of an instruction data packet. Before enabling the serial data transmission, another important information was also sent to the controller in order to settle the necessary time to reach the destination, regardless of the motor starting position. The driving algorithm was suitably designed to let the end-effector describe desired trajectories and to implement the direct and inverse kinematic model. Two Cartesian reference systems are introduced to expound the direct and inverse problem: the first reference $\tilde{O}(\tilde{x}, \tilde{y}, \tilde{z})$ is jointed to the shoulder (Fig. 1b), while the second reference $O(x, y, z)$ is jointed to the rotating base (Fig. 1c). Afterwards, the end-effector position is indicated by the point (x_4, y_4, z_4) and the end-effector orientation is denoted by φ. Moreover, l_1, l_2 and l_3 are the lengths of the three links (l_1 = 120 mm, l_2 = 128 mm, l_3 = 75 mm) and θ_0, θ_1, θ_2 and θ_3 are the rotation angles of the base (named joint 0), of the shoulder (named joint 1), of the elbow (named joint 2) and of the wrist (named joint 3) respectively.

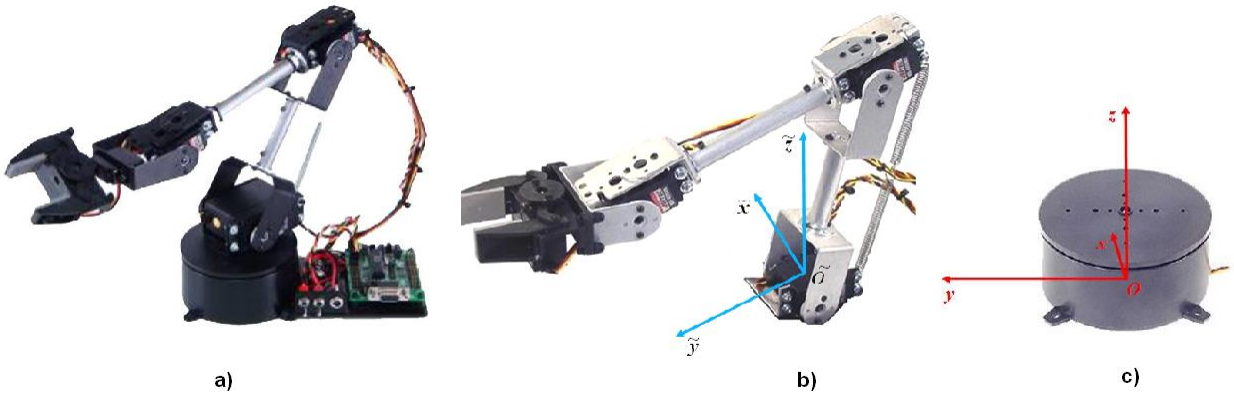

Figure 1. a) The robotic arm;b) The reference system $\tilde{O}(\tilde{x},\tilde{y},\tilde{z})$ c) The reference system $O(x,y,z)$

a. Direct kinematic model

The direct problem is to find (x_4, y_4, z_4) and φ from θ_0, θ_1, θ_2 and θ_3 [22]. The rotation angles θ_1, θ_2 and θ_3 are expressed in current reference system so that the reference system with origin in the joint 2 is obtained by rotating the joint 1 and the reference system with origin in the joint 3 is obtained by rotating the joint 1 and 2. Let us indicate by the points $(0,\tilde{y}_i,\tilde{z}_i)$ the positions of the ith joint and by $(0,\tilde{y}_4,\tilde{z}_4)$ the end-effector position with respect to the reference $\tilde{O}(\tilde{x},\tilde{y},\tilde{z})$. It is possible to obtain each joint position (Fig. 2) by simple geometrical considerations, as indicated in (1).

$$\begin{gathered}\tilde{y}_1 = 0; \quad \tilde{z}_1 = 0 \\ \tilde{y}_2 = l_1\cos\theta_1; \quad \tilde{z}_2 = l_1\sin\theta_1 \\ \tilde{y}_3 = \tilde{y}_2 + l_2\cos(\theta_1+\theta_2); \quad \tilde{z}_3 = \tilde{z}_2 + l_2\sin(\theta_1+\theta_2) \\ \tilde{y}_4 = \tilde{y}_3 + l_3\cos(\theta_1+\theta_2+\theta_3); \quad \tilde{z}_4 = \tilde{z}_3 + l_3\sin(\theta_1+\theta_2+\theta_3)\end{gathered} \tag{1}$$

The end-effector orientation φ is expressed in (2) adding together the angles θ_1, θ_2 and θ_3.

$$\varphi = \theta_1 + \theta_2 + \theta_3 \tag{2}$$

When the base joint rotates around the z axis, the point $\tilde{O}$ describes a circumference arc η having parametric equations expressed in (3), with radius p = 15 mm, lying on a plane at a level q = 67 mm. The parameter u varies from 0 to π.

$$\begin{aligned} x_\eta(u) &= p\cos u \\ y_\eta(u) &= p\sin u \\ z_\eta(u) &= q \end{aligned} \tag{3}$$

If $u = \theta_0$, the point $\tilde{O}$ has coordinates $(x_\eta(\theta_0), y_\eta(\theta_0), q)$ in the reference system $O(x, y, z)$ and the position of the i[th] joint is obtained by (4).

$$\begin{aligned} x_i &= x_\eta(\theta_0) + \tilde{y}_i \cos\theta_0 = (p + \tilde{y}_i)\cos\theta_0 \\ y_i &= y_\eta(\theta_0) + \tilde{y}_i \sin\theta_0 = (p + \tilde{y}_i)\sin\theta_0 \\ z_i &= \tilde{z}_i + q \end{aligned} \tag{4}$$

Substituting recursively (1) in (4), the end-effector position (x_4, y_4, z_4) is obtained by the equation (5)-(7).

$$x_4 = [p + l_1\cos\theta_1 + l_2\cos(\theta_1 + \theta_2) + l_3\cos(\theta_1 + \theta_2 + \theta_3)]\cos\theta_0 \tag{5}$$

$$y_4 = [p + l_1\cos\theta_1 + l_2\cos(\theta_1 + \theta_2) + l_3\cos(\theta_1 + \theta_2 + \theta_3)]\sin\theta_0 \tag{6}$$

$$z_4 = q + l_1\sin\theta_1 + l_2\sin(\theta_1 + \theta_2) + l_3\sin(\theta_1 + \theta_2 + \theta_3) \tag{7}$$

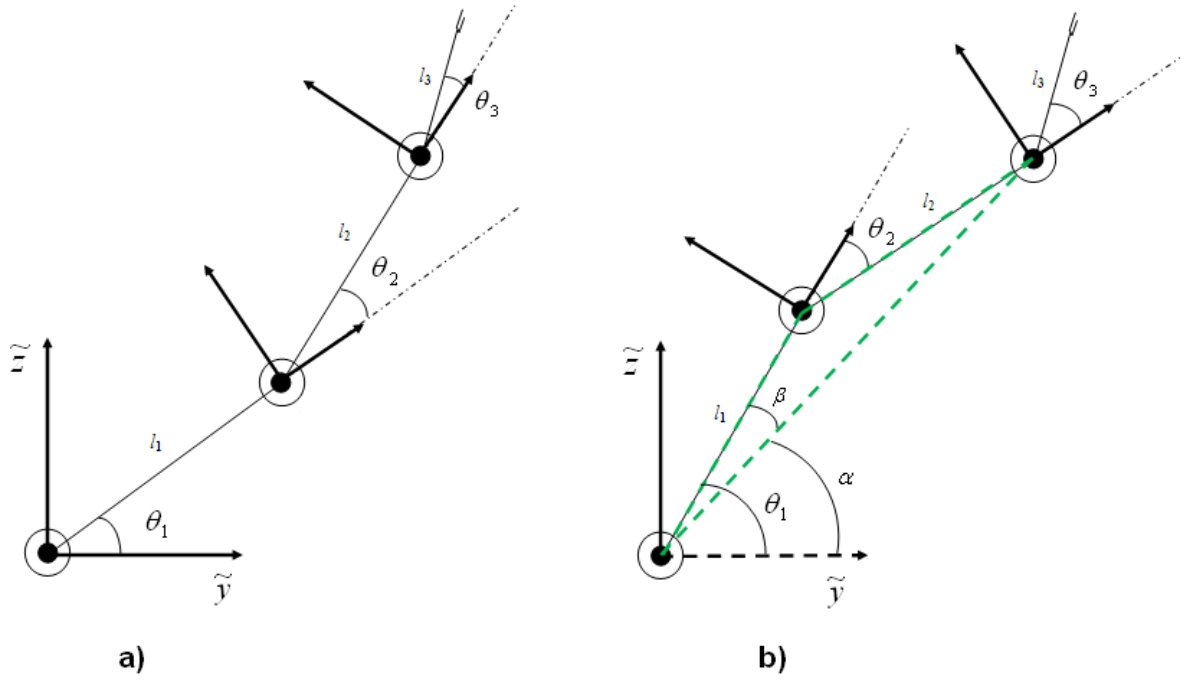

Figure 2. Scheme of the robotic arm: a) low elbow configuration; b) high elbow configuration.

b. Direct kinematic model

The inverse kinematic problem consists in the determination of the joint variables θ_0, θ_1, θ_2 and θ_3 in such a way as to obtain the end-effector desired position (x_4, y_4, z_4) and its orientation φ [22].

The orientation φ is the angle formed by the last link with respect to the y-axis when θ_0=90°. The inverse problem has two possible solutions depending on the variable θ_2 [22]. One of the solutions is relating to a negative value of θ_2 (configuration of high elbow) and the other one is relating to a positive value of θ_2 (configuration of low elbow) [22]. The choice on the elbow configuration belongs to the user that can establish how to reach the desired end-effector pose. The angle of the base joint θ_0 is calculated by (8).

$$\theta_0 = \arctan\left(\frac{y_4}{x_4}\right) \tag{8}$$

The end-effector position may be expressed in the $\tilde{O}(\tilde{x},\tilde{y},\tilde{z})$ reference system by (9) (Fig. 2a).

$$\begin{gathered}\tilde{y}_4 = \frac{y_4}{\sin\theta_0} - p, \quad \text{if } \sin(\theta_0) \neq 0 \\ \tilde{y}_4 = x_4 - p, \quad \text{if } \theta_0 = 0° \\ \tilde{y}_4 = -x_4 - p, \quad \text{if } \theta_0 = 180° \\ \tilde{z}_4 = z_4 - q\end{gathered} \tag{9}$$

The geometrical relationship referred to Fig. 2 allows the calculation of the point $(\tilde{y}_3,\tilde{z}_3)$ as in (10) and the angle θ_2 by means of (11).

$$\begin{gathered}\tilde{y}_3 = \tilde{y}_4 - l_3\cos\varphi \\ \tilde{z}_3 = \tilde{z}_4 - l_3\sin\varphi\end{gathered} \tag{10}$$

$$\cos\theta_2 = \frac{\tilde{y}_3^{\,2} + \tilde{z}_3^{\,2} - l_1^{\,2} - l_2^{\,2}}{2l_1l_2} \tag{11}$$

When calculating θ_2, we have to consider that the sign of sin(θ_2) is negative in the configuration with high elbow (Fig. 2b), whereas it is positive in the configuration with low elbow (Fig. 2a). The angle θ_1 may be obtained as in (12) (the sign "+" is for the high elbow, while the sign "-" is for the low elbow) and, finally, the angle θ_3 is given by (13).

$$\theta_1 = \operatorname{atan2}\left(\frac{\tilde{z}_3}{\tilde{y}_3}\right) \pm \arccos\left(\frac{l_1 + l_2\cos\theta_2}{\sqrt{\tilde{y}_3^{\,2} + \tilde{z}_3^{\,2}}}\right) \tag{12}$$

$$\theta_3 = \varphi - \theta_2 + \theta_1 \tag{13}$$

Since all the necessary calculations are automatically made to get information on the parameters θ_0, θ_1, θ_2 and θ_3, the user has to choice only the configuration (high or low elbow) and no further task is entrusted to it. In this way, the robotic arms operate like a human one.

Furthermore, the work space was closely examined and a database with some reachable positions was created in such a way as to define the more convenient deposit locations for the transport structures. A suitable code was implemented in Matlab [23] to let the end-effector describe appropriate trajectories by forcing its gripper to pass across different points in the reference system.

III. FEATURE EXTRACTION AND CLASSIFICATION

The used camera is an optical device able to feed coloured images to a computer by means of a Universal Serial Bus (USB) communication. Each digital coloured image has a resolution of 352×288 pixels and it is described by three matrices with elements *r*, *g*, *b* of intensities for the primary colours (red, green and blue respectively) that represent a pixel value varying in the range from 0 to 255 (0 is for red, green, or blue; 255 is for white). At first, the coloured images were acquired in condition of artificial lighting by placing and switching on a neon light in the work space. The input image was converted from the RGB into the HSI (Hue, Saturation and Intensity) space in order to obtain a grayscale image by means of the average method. This method consists in the elimination of hue and saturation information by simply averaging the elements *r*, *g*, *b*. Successively, the three matrices were converted into a single matrix whose generic element has the value 0 for black and the value 255 for white. Five grayscale images obtained by the RGB images of five different SKF ball bearings (types 629-Z, 6202N, 6203-Z, 6204, 6205-Z) [24] are illustrated in Fig. 3.

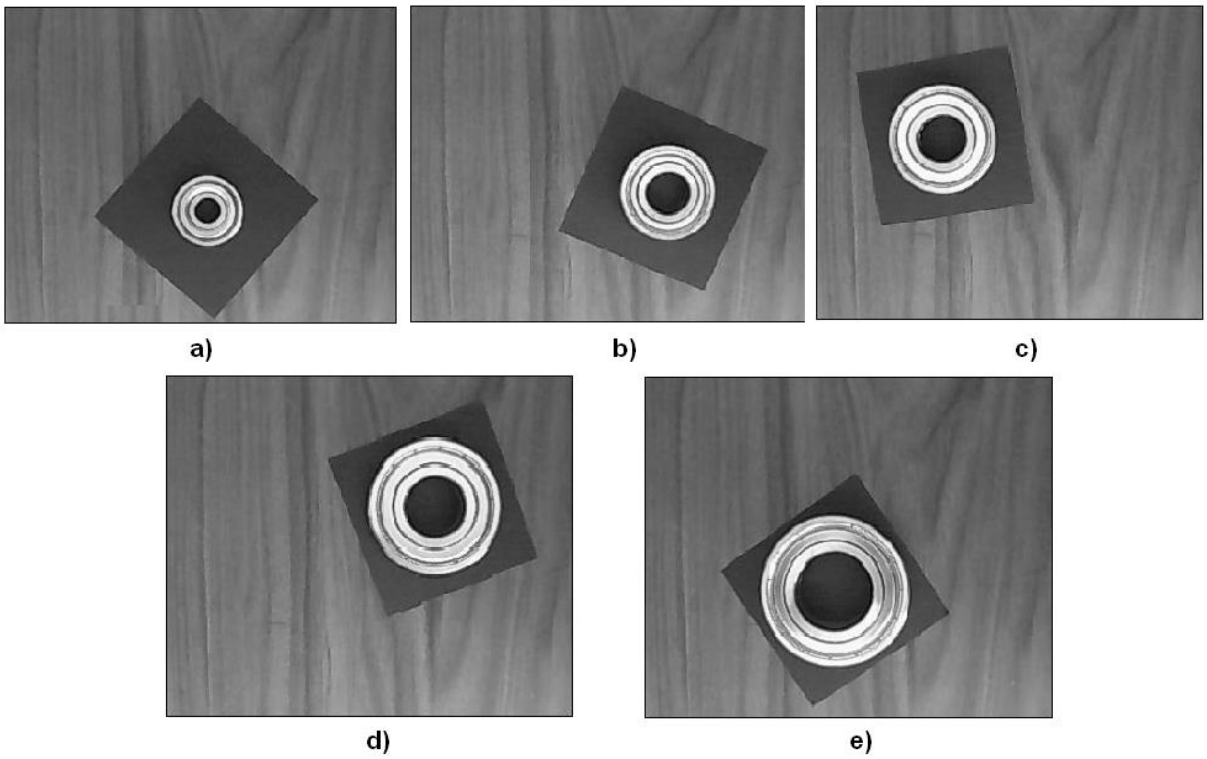

Figure 3. Grayscale intensity images: a) 629-Z; b) 6202N; c) 6203-Z; d) 6204; e) 6205-Z.

The following step was concerned with conversion of the grayscale image into black and white so as to draw a binary image. An appropriate threshold value *s* was fixed on the gray-level looking at the histogram. In particular, the main histogram peak was analysed in the experimental tests and *s* = 178 appeared to be the best choice in all cases. This optimum threshold was also automatically performed by applying the Otsu's method. Two different classes of pixels were contained in the grayscale image and so the considered method permitted to minimize the intra-class variance, that is the same as maximizing the inter-class variance. The probability of observing a grey-level is given in Fig. 4 for the two images of Fig. 3a and Fig. 3b respectively.

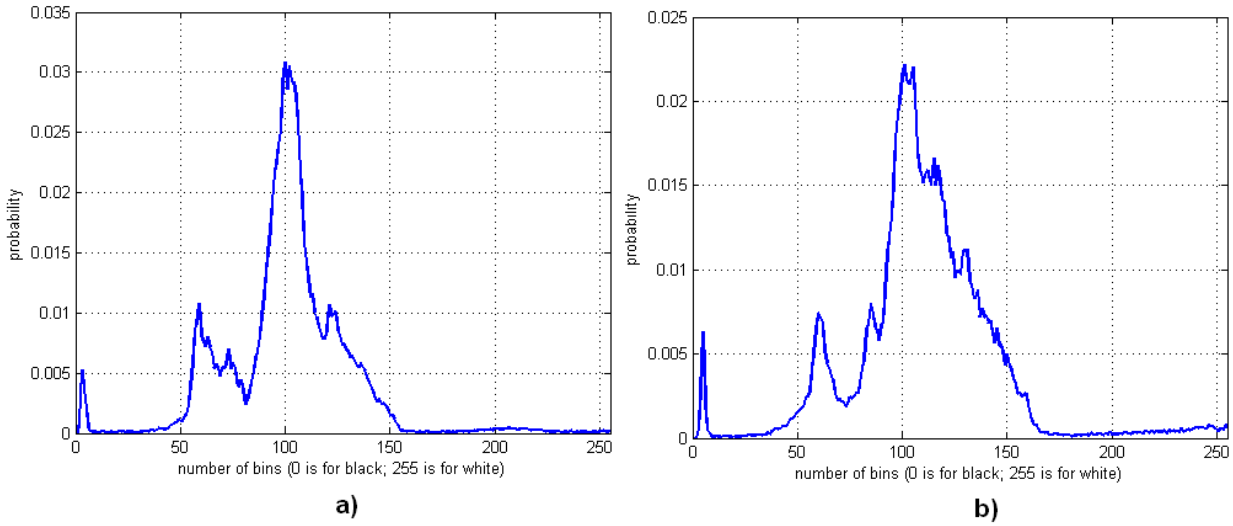

Figure 4. Probability of observing a gray-level: a) 629-Z; b) 6202N.

All the elements with value *i* less than *s* were imposed to 0 (that is relating to black) and the elements with value *i* greater than *s* were imposed to 255 (that is relating to white). After that the binary image was obtained, all the connected components having less than *n* pixels were removed and a binary image was obtained so that small sets of white pixels were excluded. The value *n*=500 and a two-dimensional eight-connected pixel connectivity assured the best filtering operation. An example of pre-filtered and post-filtered images is given in Fig. 5a) and b). Moreover, when the bearing was not located on the surface of the transport structure, a flood-fill operation was performed to extract the region concerned with such surface. This is necessary to detect the point that the end-effector has to reach in case the user wants to grip and move the structure without any bearing supported. In this situation, the binary image shows some holes, that are areas of black pixels surrounded by white pixels. The flood-fill operation changes pixels that have value 0 (black) into pixels that had value 255 (white) so as to remove unexpected black regions due to irrelevant artefacts, such as some writings inside the target surface. When the processing technique hitherto exposed is applied to the RGB image of the transport structure illustrated in Fig. 5c) the corresponding binary image is shown in Fig. 5d). One can note that such image is directly useful to measure the number of pixels concerned with the supporting surface area.

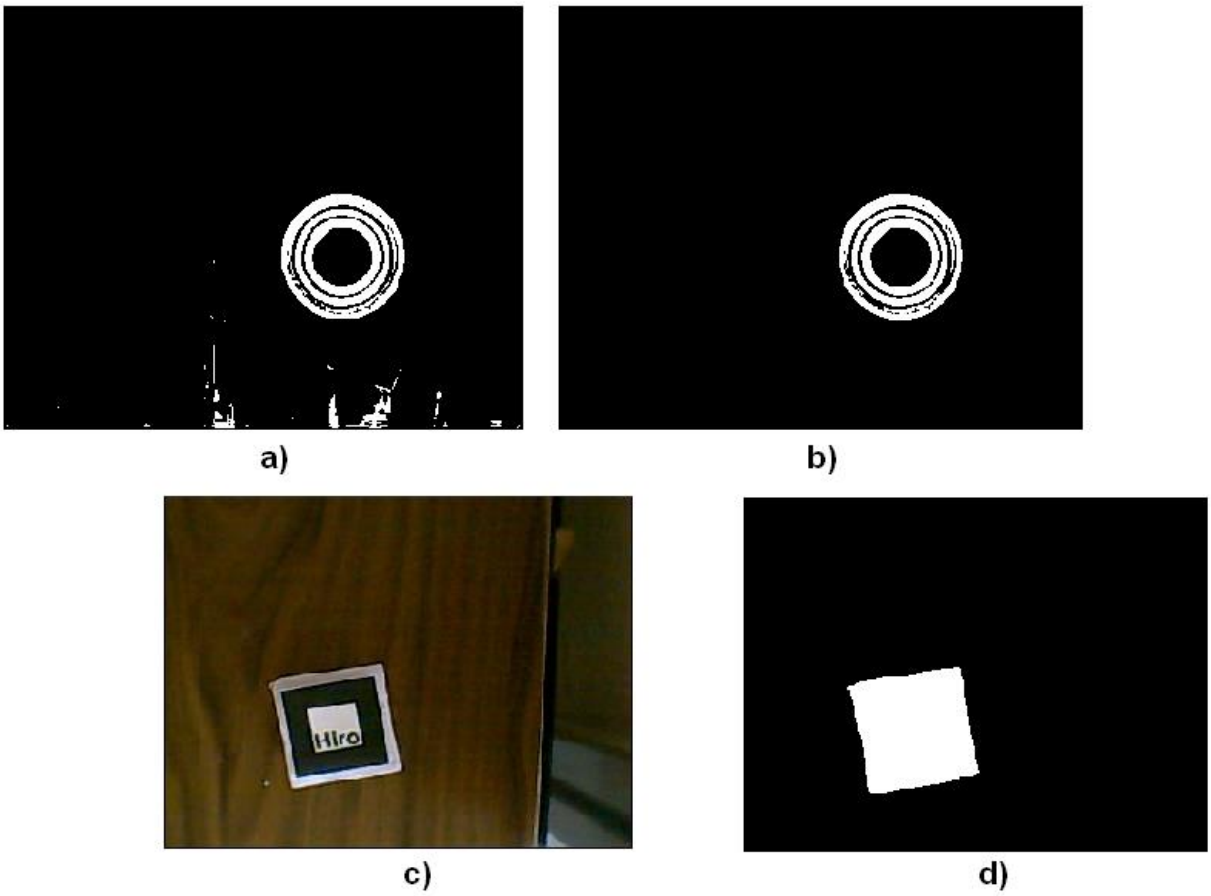

Figure 5. a) Binary image obtained by thresholding – 6202N; b) Elimination of all the connected components having fewer than 100 pixels – 6202N; c) Input image of the transport structure surface; d) Flood-fill operation performed to take off any hole.

On the contrary, in case the ball bearing lies on the supporting surface, the obtained image has to be differently enhanced for feature extraction and classification. In fact, even though the supporting surface is covered by means of a black sheet to make easier image segmentation, some undesired effects of local shadow may occur. In order to exclude all the pixels due to these phenomena, the binary image was modified by means of morphological closing with a disk-shaped structuring element. The morphological closing operation consists of a dilation followed by an erosion. Both flood-fill operation or morphological closing was realized making use of functions provided by the Image Processing toolbox in Matlab [23]. The Fig. 6 shows the output images resulting from the

application of closing. It is possible to note the effect of local shadows as concentric regions of black pixels surrounded by white pixels (see Fig. 5a and Fig. 5b).

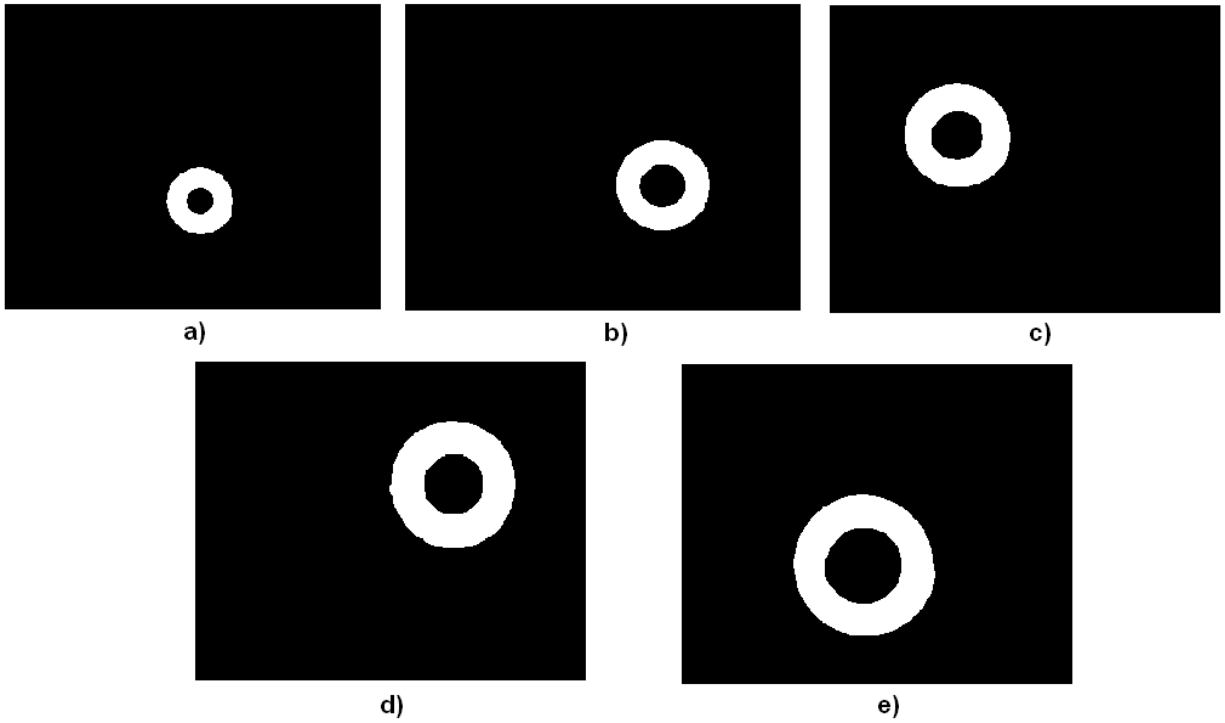

Figure 6.Morphological closing on the binary image: a) 629-Z; b) 6202N; c) 6203-Z; d) 6204; e) 6205-Z.

After morphological closing, the spurious regions were removed and the target object could be easily detected as a white ring-shaped area. The whole procedure of image processing is summarized through the flow-chart in Fig. 7. Two almost concentric and convex regions could be extracted as depicted in Fig. 8. The recognition goal is achieved by the calculation of the area of each extracted region, that is considered as number of relating pixels.

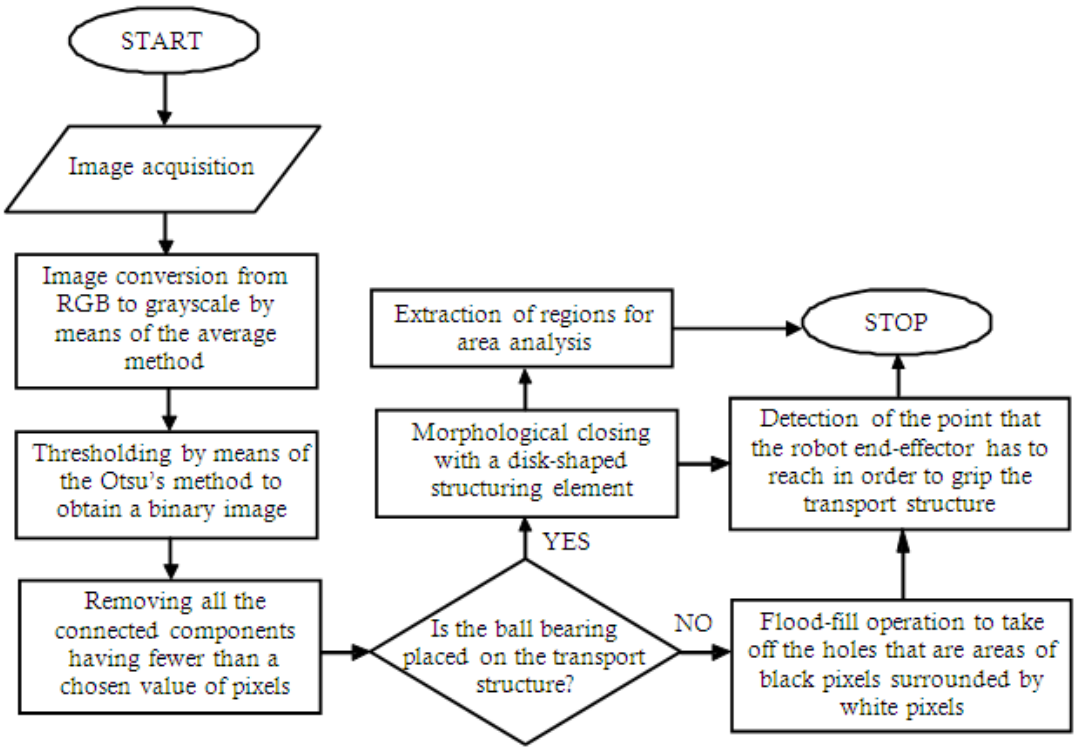

Figure 7. Flow chart describing the whole processing procedure.

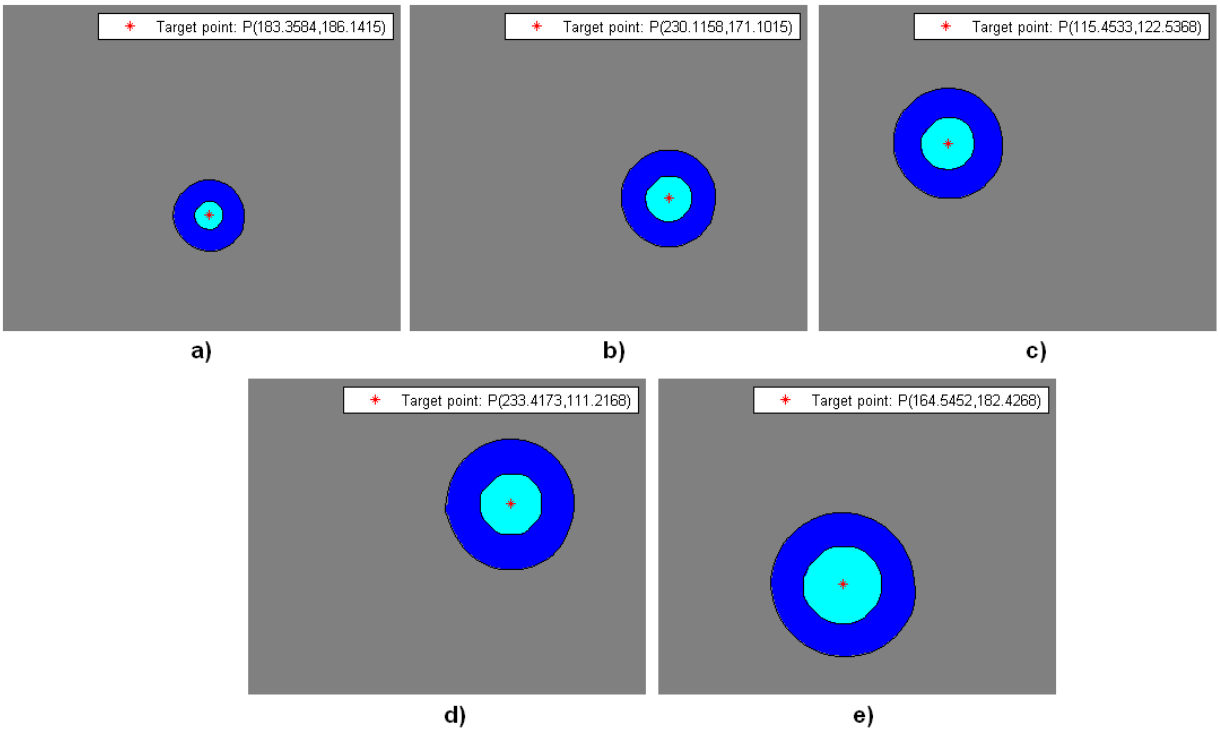

Figure 8. . Detection of the target object as convex regions: a) 629-Z; b) 6202N; c) 6203-Z; d) 6204; e) 6205-Z.

The information on the areas obtained as mean of ten values from ten processed images is given in Table 1. The first value concerns with the area of the greater circular region, whereas the second value refers to the area of the smaller circular region. The difference between these two values is the area in pixels of the ring-shaped object. This apparent area is compared with the real area in cm^2 of each ball bearing in Table 1.

Table 1:Comparison of the apparent area with the real area for the different types of ball bearings.

Type of SKF ball bearing	**Mean areas of the two convex regions as number of pixels**	**Object area as difference of the two obtained areas in pixels**	**Real area in cm^2**
629-Z	3080.60 494.20	2586.4	4.67
6202N	5637.50 1323.60	4313.9	7.85
6203-Z	7383.60 1694.60	5689.0	10.30
6204	10283.00 2339.10	7943.9	14.21
6205-Z	12704.00 3725.30	8978.7	16.33

The areas in pixels strictly depend on the distance between the camera and the target object that was firstly fixed at about 28 cm. In this case, the authors could ascertain that 550 pixels approximately correspond to a real area of 1 cm^2. In other words, when the distance camera-object is d = 28 cm, one pixel correspond to u = 0.0426 cm in the considered image. The small differences in the thickness of each type of ball bearing did not entail a significant variation of pixels per centimetre. For the sake of evaluating the relationship between u and d at changing the depth between the camera and the object, several experimental tests were carried out and the inverse-linear function in (14) was obtained.

$$u = 0.00152 \cdot d, \quad d \in [23,28]cm \tag{14}$$

In all experiments for the calculation of *u* from *d*, the object was vertically centred with respect to the optical axis and the object-glass laid on a plane that was parallel to the support plane. However, the images had such a resolution that the formula could be roughly utilized in case of decentralization in the distance range from 23 to 28 cm. The values of Table 1 can be suitably transformed according to the camera depth by (14).

In this way, the recognition directly comes from the matching between the area features of a new test image and the stored database. Moreover, there is to highlight that the centroids of the considered regions provide information on the target point (x_4, y_4, z_4) that the robotic arm has to reach for gripping the transport structure. Several experimental tests were carried out with the five different ball bearings and both correct classification and end-effector positioning were proved in the experimental condition of neon lighting. In order to show that the common techniques based on Hu moment invariants cannot be used to recognize the ball bearings, the authors calculated the seven invariants that are independent from scale, translation and rotation. At this aim, the post-processing binary image $f(a,b)$ was considered to draw the Hu moment invariants as functions of central moment invariants [1-3]. The raw moments of order $\alpha+\beta$ were calculated by (15) and the derived object properties could be verified: M_{00} is the area of each object; $\bar{a} = M_{10}/M_{00}$ and $\bar{b} = M_{01}/M_{00}$ are the centroid coordinates.

$$M_{\alpha\beta} = \sum_a \sum_b a^\alpha b^\beta f(a,b) \tag{15}$$

The area M_{00} slightly differs from the area obtained as difference between the areas of the two almost concentric and circular regions. That is why the extracted regions have boundary closed curves that are convex. The values μ for M_{00} obtained as mean of ten values from ten images of each bearing are given in Table 2 and Fig. 9 (the same set used for the values of Table 1 is considered). The standard deviation σ and the relative standard deviation values were also calculated to appreciate the dispersion from the average and shown in Table 2 and Fig. 10; in Table 2 also a possible a separation range [μ-5 σ μ+5 σ] between the different ball bearings is shown. One can note that the standard deviation is very low for M_{00} so confirming that the areas are good descriptors.

Table 2:Statistical properties of M_{00} for the different types of ball bearings.

Type of SKF ball bearing	**Mean value μ of M_{00}**	**Standard deviation σ of M_{00}**	**Relative standard deviation (σ/μ)x100% of M_{00}**	**μ-5σ**	**μ +5σ**
629-Z	2551.30	23.26	0.91	2435.01	2667.59
6202N	4335.20	43.05	0.99	4119.95	4550.45
6203-Z	5640.80	48.97	0.87	5395.95	5885.64
6204	7861.70	43.24	0.55	7645.49	8077.92
6205-Z	8898.20	42.34	0.47	8686.50	9109.90

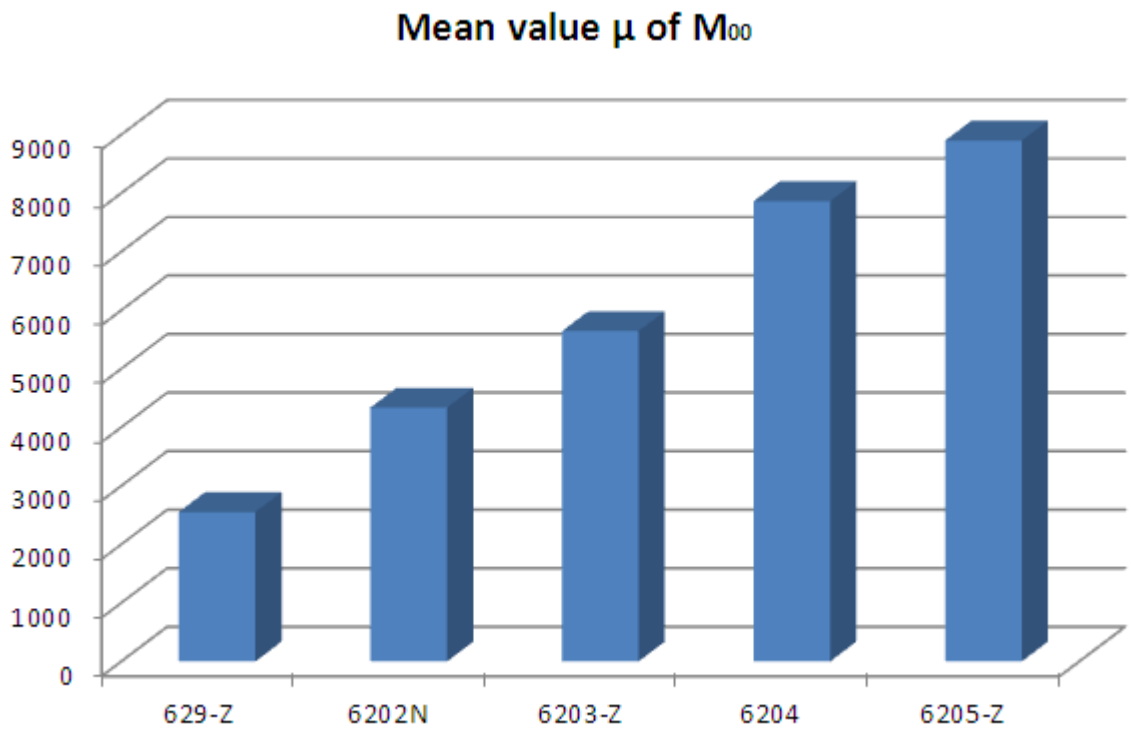

Figure 9. . Mean value of the zero-order raw moment.

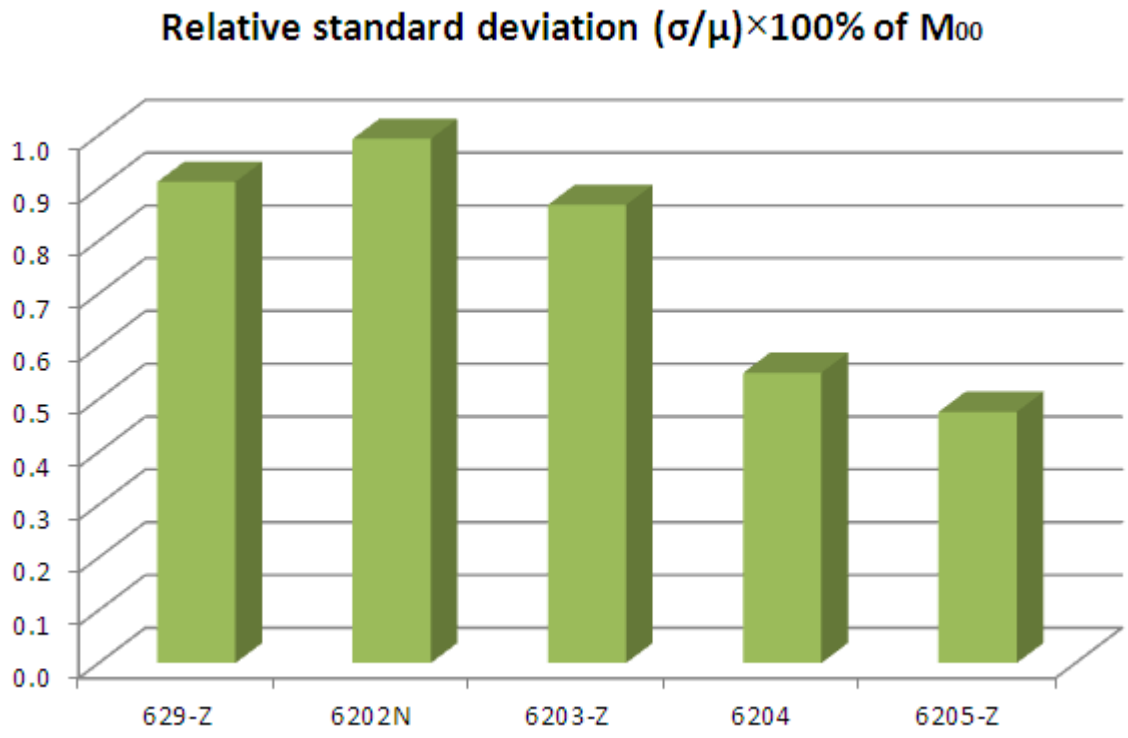

Figure 10. Standard deviation of the zero-order raw moment.

After calculating the raw moments, the central moment invariants to both translation and changes in scale were obtained by (16) for $\alpha+\beta \geq 2$.

$$\eta_{\alpha\beta} = M_{00}^{-\left(1+\frac{\alpha+\beta}{2}\right)} \sum_{a}\sum_{b} (a-\bar{a})^{\alpha} (b-\bar{b})^{\beta} f(a,b) \tag{16}$$

The mean values for η_{20} and η_{02} are reported in Table 3 and in Table 4 respectively. They are referred to the ten previously considered images. Furthermore, the standard deviation ,the relative standard deviation values and the possible separation range [μ-5 σ μ+5 σ] are added to the considered tables. It was obtained that higher order central moment invariants were not able to permit to distinguish the different bearings.

Table 3:Statistical properties of μ_{20} for the different types of ball bearings.

Type of SKF ball bearing	**Mean value μ of μ_{20}**	**Standard deviation σ of μ_{20}**	**Relative standard deviation (σ/μ)x100% of μ_{20}**	**μ-5σ**	**μ +5σ**
629-Z	0.11048	0.00069	0.62861	0.10701	0.11395
6202N	0.12884	0.00129	0.99787	0.12242	0.13527
6203-Z	0.12756	0.00232	1.81795	0.11596	0.13915
6204	0.12884	0.00236	1.83329	0.11703	0.14065
6205-Z	0.14692	0.00152	1.03572	0.13931	0.15453

Table 4:Statistical properties of μ_{02} for the different types of ball bearings.

Type of SKF ball bearing	**Mean value μ of μ_{02}**	**Standard deviation σ of μ_{02}**	**Relative standard deviation (σ/μ)x100% of μ_{02}**	**μ-5σ**	**μ +5σ**
629-Z	0.10934	0.00166	1.51661	0.10105	0.11763
6202N	0.12467	0.00103	0.82898	0.11950	0.12983
6203-Z	0.12596	0.00128	1.01902	0.11954	0.13237
6204	0.12450	0.00118	0.94497	0.11862	0.13038
6205-Z	0.14452	0.00171	1.18527	0.13596	0.15308

Finally, the Hu invariants were calculated by (17).

$$
\begin{aligned}
H_1 &= \eta_{20} + \eta_{02} \\
H_2 &= (\eta_{20} - \eta_{02})^2 + 4\eta_{11}^{\ 2} \\
H_3 &= (\eta_{30} - 3\eta_{12})^2 + (3\eta_{21} - \eta_{03})^2 \\
H_4 &= (\eta_{30} + \eta_{12})^2 + (\eta_{21} + \eta_{03})^2 \\
H_5 &= (\eta_{30} - 3\eta_{12})(\eta_{30} + \eta_{12})[(\eta_{30} + \eta_{12})^2 - 3(\eta_{21} + \eta_{03})^2] + \\
&\quad (3\eta_{21} - \eta_{03})(\eta_{21} + \eta_{03})[3(\eta_{30} + \eta_{12})^2 - (\eta_{21} + \eta_{03})^2]
\end{aligned}
\tag{17}
$$

$$H_6 = (\eta_{20} - \eta_{02})[(\eta_{30} + \eta_{12})^2 - (\eta_{21} + \eta_{03})^2] + 4\eta_{11}(\eta_{30} + \eta_{12})(\eta_{21} + \eta_{03})$$

$$H_7 = (3\eta_{21} - \eta_{03})(\eta_{30} + \eta_{12})[(\eta_{30} + \eta_{12})^2 - 3(\eta_{21} + \eta_{03})^2] - (\eta_{30} - 3\eta_{12})(\eta_{21} + \eta_{03})[3(\eta_{30} + \eta_{12})^2 - (\eta_{21} + \eta_{03})^2]$$

The Hu moment invariants do not permit to distinguish an object from another one because the considered ball bearings have the same shape. According to the general theory recently developed in [4,6,8], a further third order moment invariant was also calculated by (18). This allowed to complete the set with the missing independent element H_8 and to prove the dependency of H_3 from H_5, H_7 and H_4; H_8 is equal to $(H_5^2+H_7^2)/H_4^3$ [4,6,8].

$$H_8 = \eta_{11}[(\eta_{30} + \eta_{12})^2 - (\eta_{03} + \eta_{21})^2] - (\eta_{20} - \eta_{02})(\eta_{30} + \eta_{12})(\eta_{03} + \eta_{21}) \quad (18)$$

The moments H_j (j=1,..,8) are invariant to translation, scaling and rotation and, as expected, none of them provided any discrimination power because of the circular symmetry [6]. On the other hand, the moment H_1, depending on η_{20} and η_{02}, could be considered to perceive an eventual erroneous shape evaluation. The obtained mean values for H_1 and the relating standard deviations and separation intervals are given in Table 5. The relative standard deviation was less than 0.8%. When the work space is artificially lighted up, the threshold value s = 178 allows to extract the two convex regions for areas analysis. In this case, the new values obtained for H_1 were always within the interval [0.211, 0.299], according to the evaluation of confidence in Table 5.

Table 5:Statistical properties of H_1 for the different types of ball bearings.

Type of SKF ball bearing	**Mean value μ of H_1**	**Standard deviation σ of H_1**	**Relative standard deviation (σ/μ)x100% of H_1**	**μ-5σ**	**μ +5σ**
629-Z	0.21982	0.00171	0.77784	0.21127	0.22837
6202N	0.25351	0.00058	0.22977	0.25060	0.25642
6203-Z	0.25351	0.00122	0.48042	0.24742	0.25960
6204	0.25333	0.00132	0.52269	0.24671	0.25995
6205-Z	0.29144	0.00150	0.51458	0.28394	0.29894

After conducting several tests in this experimental condition, the authors decided to appraise the performance of the proposed approach at changing brilliance. They switched off the neon light and then they used the camera to take images with the sun light coming through the windows. Because of low-light effects, it was possible to appreciate that the extraction of two regions failed for s = 178 in most cases. In those occasions, on applying the Otsu's method, a new threshold value could be obtained but the purpose of correct classification was not always achieved. Non-homogeneous image zones of different intensity could be responsible for unexpected binary image and consequently for incorrect region extraction as shown in Fig. 11a) and b) respectively. The considered images were obtained by processing a photo taken to the bearing 6204. The obtained values for M_{00}, η_{20}, $\eta 02$ and H_1 are pointed out in Table 6.

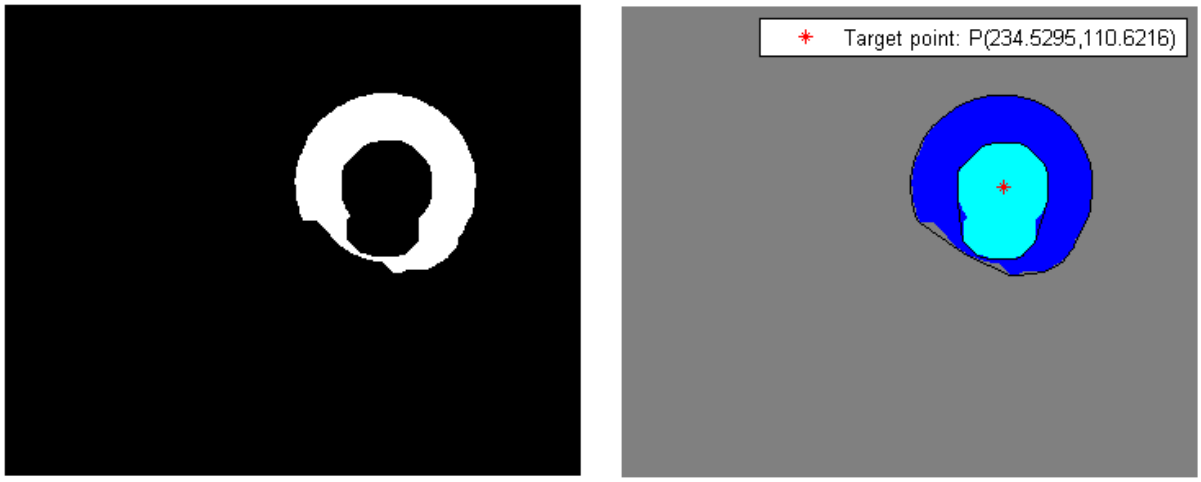

Figure 11. a) Unexpected binary image; b) incorrect region extraction.

Table 6:Moments in condition of low-lighting for ball bearing type 6204.

"condition of low-lighting" ball bearing	M_{00}	μ_{20}	μ_{02}	H_1
6204	6001	0.1389	0.1759	0.3148

Although the boundary curves of the two regions approximately appear concentric, they are not almost circular. This erroneous shape detection could be simply detected by looking at the H_1 value given in Table 5, equal to about 0.315, greater than 0.299. The obtained M_{00} value was 6001 pixels,

that is close to the expectation for the bearing 6203-Z, so that the object could be misclassified. However, the considered value is outside any 99.99% confidence interval (see Table 2) and the only M_{00} information is enough to discover the failure in this case.

IV. EXPERIMENTAL USE OF THE ROBOTIC ARM AND SORTING WITH RFIF SUPPORT

The almost concentric regions lie on a plane that is perpendicular to the pointing direction of the camera. The target point (x_4, y_4, z_4) is calculated as the mean point of the two obtained centroids. This point is depicted as a red star point in Fig. 8 with respect to the camera reference system $O_c(x_c,y_c)$. This reference system has origin O_c in the upper-left pixel, the x_c axis is horizontal and goes left-to-right, whereas the y_c axis is vertical and goes from up to down. Since the camera resolution is 352×288, the number of pixel rows is 288 (maximum y_c value) and the number of pixel columns is 358 (maximum x_c value). Let us indicate by (x_c^t, y_c^t) the target point with respect to the reference $O_c(x_c,y_c)$, as labelled in Fig. 12.

The relationship in (14) permitted to obtain the transformation from the camera reference system $O_c(x_c,y_c)$ to the robot reference system $O(x,y)$, as shown in (19), where (x_o, y_o) = (2.7, 26.6) is the upper-left pixel point expressed with respect to $O(x,y)$ (the unit is cm). The gripping level was chosen in consequence of the height of the transport structure and fixed at z_4 = 4 cm in all the experiments

$$x_4 = x^0 - ux_c^{\ t}; \quad y_4 = y^0 + uy_c^{\ t} \tag{19}$$

In order to check the successful events in recognition, the authors appealed to RFID technology [25] and so they took real advantage of an automatic control system able to interpret the outcome of image processing. The integration between camera and RFID was a convenient way to speed up the verification process. Moreover, there is to consider that an inexpert human eye could confuse a ball bearing from another one owing to the close resemblance. RFID devices have recently become very popular in robotic applications and consist of two fundamental elements: the tag and the reader. The tag is a small dimension element composed of an antenna and a microchip, whereas the reader is a greater element capable of questioning the tag through one or more antennas by looking for the unique identification code stored in the microchip. In all the tests, one tag was stuck on the base of each transport structure and the reader was placed in an appropriate location in the work space. In this way, it was possible to manage the robotic arm by moving the transport structure

from a starting position to a final one. In the simplified application sketched in Fig. 12, the starting position is indicated with Pos 0, while the final position could be chosen between two different possibilities, indicated as Pos 1 and Pos 2 respectively.

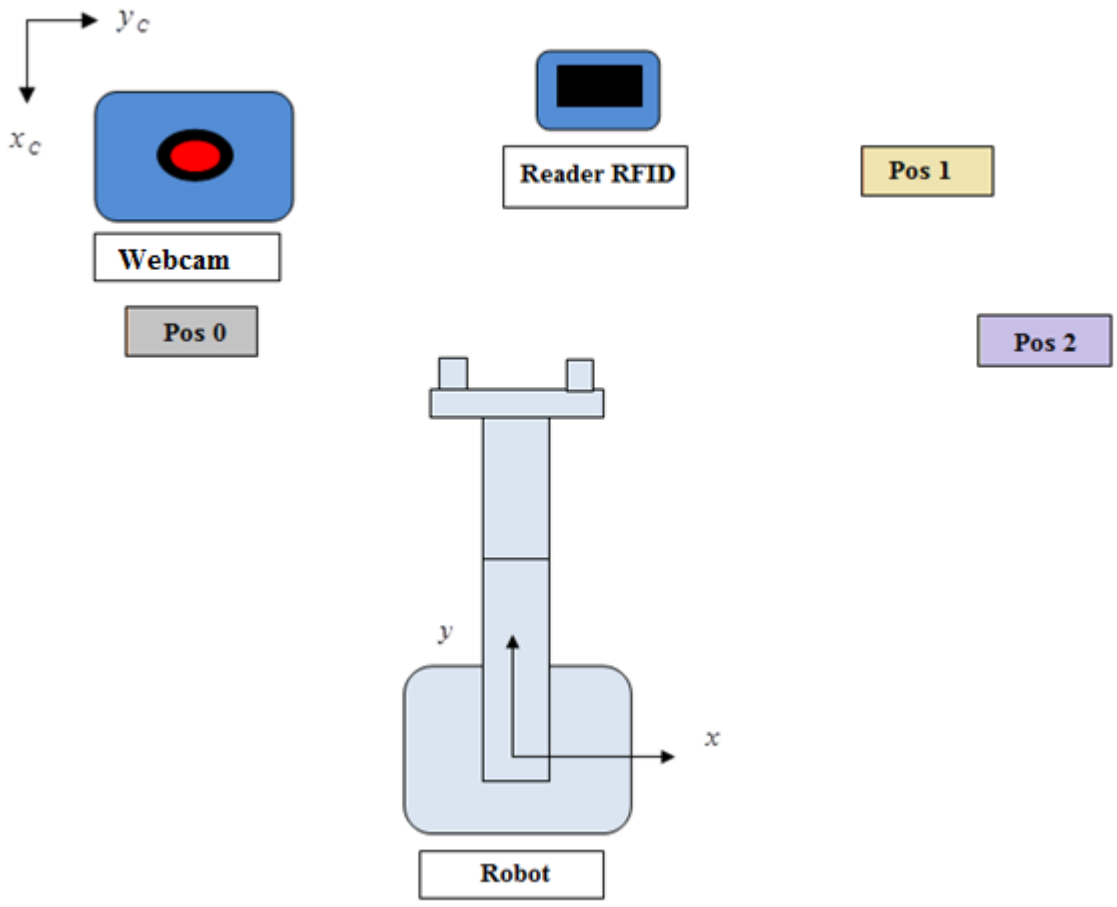

Figure 12. The scheme of the experimental setup.

The two different positions depend on the tag identification code. In the experiments, the starting position Pos 0 was not fixed, but it corresponded to (x_4, y_4, z_4). The camera was screwed up a slide guide above the table, where the objects were located, as illustrated in Fig. 13a. The transport structure is shown in Fig. 13b and the tag is glued as pictured in Fig. 13c. Each end-effector trajectory was planned by imposing that the transport structure passed from a point above the reader at a short distance of about 2 cm. After reaching this positioning, the end-effector was stopped for a very short time of about 0.5 seconds, that is enough for reading the information included in the

tag. The photos of the results of one of the experiments are shown in Fig. 14, where two identical objects are placed on the table in succession. The first object has a tag that contains the useful information to leads it to the position named Pos 2. On the contrary, the second object has a tag containing the information that it has to be moved to the position named Pos 1.

Figure 13. a) The used camera; b) The transport structure; c) The tag stuck on the base of the transport structure.

In real industrial applications, we can imagine that a human operator rests objects on generic positions on the table, similarly to what a belt conveyor does for distributing spare parts. All the procedure herein explained is then necessary to make automatic recognition and sorting. A suitable code elaborates the camera image in such a way as to estimate the position of the first object in the O(x,y,z) reference system (Fig. 14a). Successively, the end-effector approaches the first object, grasps it and moves it above the reader. Finally, the object is left to the final position depending from the tag information (Pos 2 in the example of Fig. 14b). Soon after, the robotic arm is moved again to the starting position and it goes to pick the second object (Fig. 14c) after that its position has been also estimated. There is to underline that the chosen final positions are outside the vision area of the webcam and so there is not confusion between the released object and the target one. According to the information contained in its tag, the second object is moved to Pos 1, as depicted in Fig. 14d. The whole operating is very quick and it takes only few seconds.

Many experimental tests demonstrated the robustness and simplicity of the proposed approach. For example, when a situation like that in Fig. 11 occurs, the incorrect area information is confirmed by the H_1 moment invariant and the anomaly is automatically detected by means of RFID. There

is to consider that RFID assures the desired assignment that will be otherwise impossible in these cases. Since a single reader may simultaneously manage dozens of tags, the classification problem can be supported in most cases.

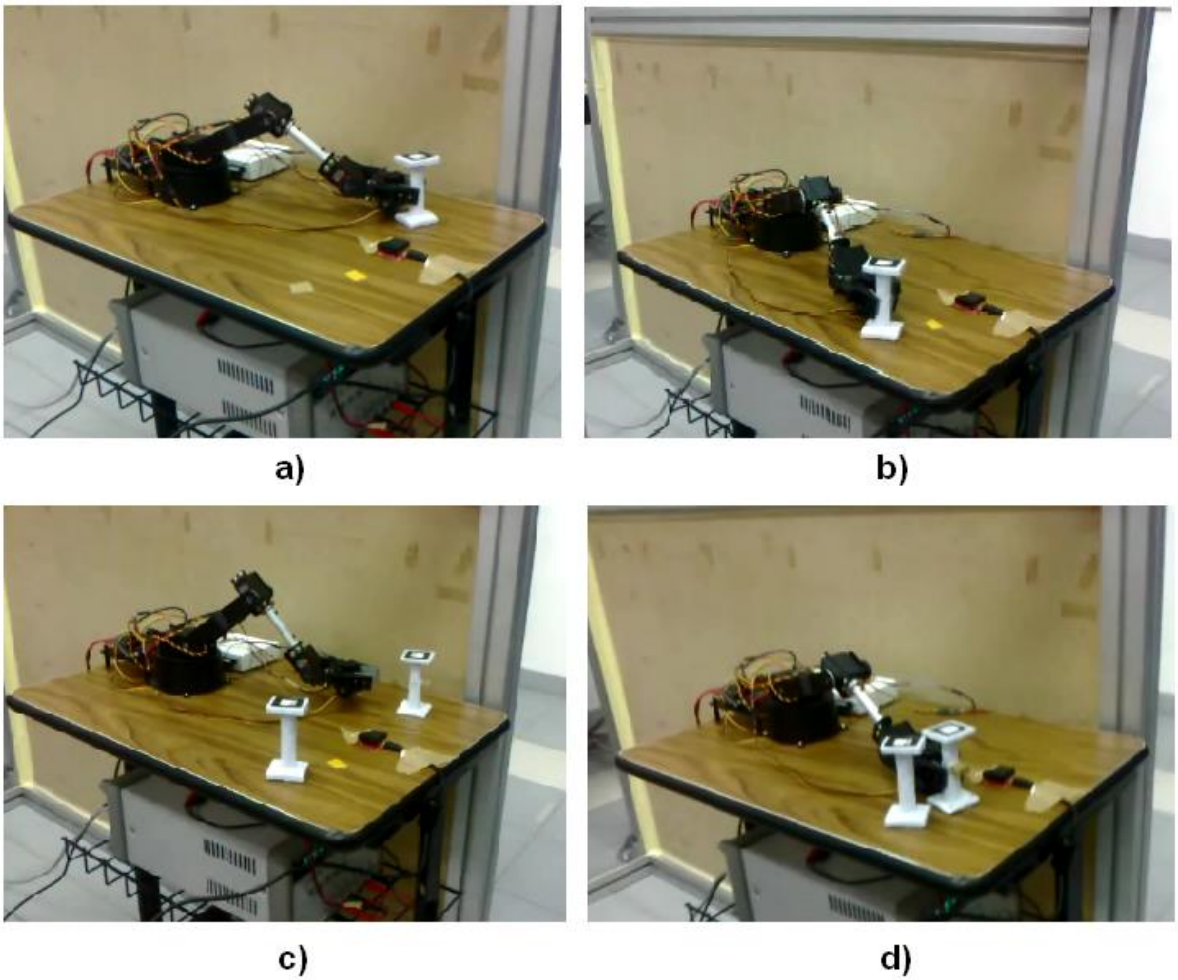

Figure 14. a) The robotic arm grasps the first object; b) The first object is moved to Pos 2; c) The arm is going to grasp the second object; d) The second object is moved to Pos 1.

VI. CONCLUSIONS

In this work a strategy of size measurements of image regions is presented to recognize different ball bearings. The objects are classified with the aim of sorting them by means of a robotic arm. In the proposed application some ball bearings are caught by the end-effector of a controlled manipulator and they are moved to appropriate locations according to the processed information

from a camera. The common recognition techniques consist in calculating moment invariants, such as Hu moments, that are descriptors independent from scale, translation and rotation. But the considered objects have all the same shape and the same colour. This condition makes more complex the classification problem that could be only solved by means of the calculation of region areas. In the early tests, the authors used an artificial neon-based lighting in order to avoid brilliance variations. They could appreciate the success in recognition in any case and automatically verify it with RFID technology. When the artificial light was switched off, the aim of correct recognition could fail owing to light variations. In some cases, it was not possible to extract two almost concentric and circular regions because small threshold variations caused significant differences in the binary image. In other cases, two almost concentric regions could be anyhow extracted but the recognition failed because their boundary curves and the concerning area values did not correspond to the expected ones. These undesired phenomena could be individualized by evaluating the first Hu moment invariant calculated. Moreover, the RFID support permitted to automatically select these failures and it anyway assured the correct assignment. The authors believe that the suggested strategy could be applied to track spare parts in assembly lines so as to improve flexible manufacturing systems. In particular, the proposed approach is specific for objects having the same shape and the same colour, such as the ball bearings, but also rings, trimmings and gaskets may be considered. Another remarkable aspect of interest is the possibility to make a robotic smart and able to perceive the objects by using very inexpensive devices.

REFERENCES

[1] Hu, M.K.: 'Visual Pattern Recognition by Moment Invariants' Transactions on Information Theory, 1962, 8, (2), pp. 179-187.

[2] Leng, J., Huang, Z.: ‘On analysis of circle moments and texture features for cartridge images recognition' Expert Systems with Applications, 2012, 39, pp. 2092-2101.

[3] Wang Yan, Z.X.: 'Leaf Image Recognition Technology Research Based on Hu Invariant Moments' Intelligent Control System and Its Application, 2011, 6, pp. 70-72.

[4] Flusser, J.: 'On the independence of rotation moment invariants' Pattern Recognition, 2000, 33, pp. 1405-1410.

[5] Mercimek, M., Gulez, K., Mumcu, T.V.: 'Real object recognition using moment invariants', Sadhna, 2005, 30, (6), pp. 765-775.

[6] Flusser, J., Suk, T.: 'Rotation moment invariants for recognition of symmetric objects' IEEE Transactions on Image processing, 2006, 15, (2), pp. 3784-3790.
[7] Rizon, M., Yazid, H., Saad, P., Shakaff, A.Y.M., Saad, A.R., Mamat, M.R., Yaacob, S., Desa, H., Karthigayan, M.: 'Object detection using geometric invariant moment' American Journal of Applied Sciences, 2006, 2, (6), pp. 1876-1878.
[8] Flusser, J., Suk, T., Zitova, B.: 'Moments and moment invariants in pattern recognition' (John Wiley & Sons, Ltd., UK, 2009).
[9] Mindru, F., Tuytelaars, T., Gool, L.V., Moons, T.: 'Moment invariants for recognition under changing viewpoints and illumination', Computer Vision and Image Understanding, 2004, 94, pp. 3-27.
[10] Chonga, C., Raveendranb, P., Mukundan, R.: 'Translation invariants of Zernike moments' Pattern Recognition, 2003, 36, pp. 1765-1773.
[11] Belkasim, S., Hassan, E., Obeidi, T.: 'Explicit invariance of Cartesian Zernike moments' Pattern Recognition Letters, 2007, 28, pp. 1969-1980.
[12] Chen, B.J., Shu, H.Z., Zhang, H., Chen, G., Toumoulin, C., Dillenseger, J.L., Luo, L.M.: 'Quaternion Zernike moments and their invariants for color image analysis and object recognition' Signal Processing, 2012, 92, 308-318.
[13] Chonga, C., Raveendranb, P., Mukundan, R.: 'Translation and scale invariants of Legendre moments' Pattern Recognition, 2004, 37, pp. 119-129.
[14] Hosny, K.M.: 'Refined translation and scale Legendre moment invariants' Pattern Recognition Letters, 2010, 31, pp. 533-538.
[15] Mukundan, R.: 'Radial Tchebichef invariants for pattern recognition', Proc. of IEEE TENCON Conference, Melbourne, Australia, November 2005, pp. 2098-2103.
[16] Xiao, B., Maa, J.F., Cui, J.: 'Radial Tchebichef moment invariants for image recognition' Journal of Visual Communication and Image Representation, 2012, 23, pp. 381-386.
[17] Assaad, M., Yohannes, I., Bermak, A., Ginhac, D., Meriaudeau F. ‘ Design and characterization of automated color system’ International Journal on Smart Sensing and Intelligent Systems, March 2014, Vol. 7 n.1 pp 1-12.
[18] Szabò, R., Lie, I.: 'Automated Colored Object Sorting Application for Robotic Arms' Proc. of 10th International Symposium Electronics and Telecommunications (ISETC), Timisoara, Romania, November 2012, pp. 95-98.
[19] Nkomo, M., Collier, M.: 'A Color-Sorting SCARA Robotic Arm' Proc. of 2nd International Conference on Consumer Electronics, Communications and Networks (CECNet), Yichang, China, April 2012, pp. 763-768.
[20] 'Lynxmotion robotic arms', http://www.lynxmotion.com.
[21] Giannoccaro, N.I., Spedicato, L., Lay-Ekuakille, A.: 'A smart robotic arm for automatic sorting of objects with different tags' Proc. of the 4th Imeko TC19 Symposium on Environmental

Instrumentation and Measurements Protecting Environment, Climate Changes and Pollution Control, Lecce, Italy, June 2013, pp. 95-98.

[22] Siciliano, B., Sciavicco, L., Villani, L., Oriolo, G.: 'Robotics – Modelling, Planning and Control' (Springer-Verlag Advanced Textbooks in Control and Signal Processing Series, London, U.K., 2009).

[23] 'Mathworks, R2012b', http://www.mathworks.it.

[24] 'SKF', http://www.skf.com/group/splash/index.html.

[25] Syamsuddin I., F. 'State of the art on secure and low cost RFID authentication protocols for RFID based vehicle license plate', International Journal on Smart Sensing and Intelligent Systems, December 2013, Vol.6 n.5 pp 1949-1969.